PCCP

ROYAL SOCIETY OF CHEMISTRY

PAPER

Published on 20 October 2026
Licensed under CC-BY 4.0

Check for updates

Cite this: DOI: 10.1039/d6cp02166b

Aggregation-activated delayed and two-photon fluorescence in a charge-modulated pyridine–acridan luminophore

Rasa Keruckiene, *[a] Kaspars Leduskrasts,[b] Ho-Chia Tsai,[c] Mariia Stanitska,[a] Daiana Ospanova,[a] Dmytro Volyniuk,[a] Edgars Suna,[b] Shi-Wei Chu[c] and J. V. Grazulevicius[a]

Molecular charge modulation offers a promising strategy for controlling the excited-state properties and aggregation behavior of organic luminophores. Nevertheless, the consequences of cationization strongly depend on the molecular structure. Herein, we investigate a twisted π-extended pyridine–dimethylacridan derivative (**PyAcr**) and its cationic pyridinium analogue (**PyAcr$^+$**) to elucidate how neutral-to-cationic transformation affects their photophysical properties. Experimental characterization combined with theoretical calculations provides insight into the relationship between molecular structure, charge distribution, excited-state character, and emission behavior. **PyAcr** exhibits aggregation-induced delayed fluorescence (AIDF), accompanied by a moderate photoluminescence quantum yield of 45% and strong two-photon-excited fluorescence (TPEF) under near-infrared excitation. In contrast, conversion of **PyAcr** to **PyAcr$^+$** alters its aggregation behavior and results in substantially weakened emission, likely reflecting the combined effects of cation formation and the structural modification introduced upon quaternization. Both derivatives exhibit high thermal stability, with onset temperatures of thermal degradation above 360 °C, good electrochemical stability, and small singlet–triplet energy gaps of 0.07–0.13 eV. Overall, the results demonstrate that cationization alone does not necessarily enhance luminescence and that the interplay between molecular charge, electronic coupling, and aggregation is critical for controlling excited-state dynamics. These structure–property relationships provide useful guidelines for the rational design of environment-responsive luminophores, while **PyAcr** shows promise as a two-photon-excited probe for bioimaging.

Received 9th June 2026,
Accepted 12th October 2026

DOI: 10.1039/d6cp02166b

rsc.li/pccp

Introduction

Due to their tunable electronic structures, low toxicity, and synthetic modularity, purely organic emissive molecules (luminophores) have become central to the development of advanced photonic applications, such as organic light-emitting diodes (OLEDs),[1,2] nonlinear-optical materials,[3–5] and high-contrast bioimaging probes.[6,7] A key advantage of organic luminophores lies in the ability to fine-tune their photophysical properties through molecular engineering, particularly by systematically varying the strength and nature of donor (D) and acceptor (A) units within a conjugated scaffold, influencing the energy levels, charge transfer (CT) character, and nonradiative decay pathways. One powerful strategy to amplify A strength is to convert a neutral heterocyclic acceptor (*e.g.*, pyridine, imidazole, triazole) into a cationic species.[8,9] This transformation introduces a positive charge, amplifying the electron-withdrawing power of A and thereby modulating the overall electronic distribution of the luminophore. Additionally, such cationization could possibly improve the molecule's ability to harvest triplet excitons[10] and interact with multiphoton excitation sources,[11] making it highly attractive for bioimaging. In a highly twisted D–A setup, conversion of a neutral pyridine to a cationic pyridinium A$^+$ substantially alters the molecular polarization and electronic structure, which can influence the nonlinear optical response in conjunction with molecular conjugation and twisting.[12] This shift can amplify the two-photon absorption (2PA) cross-section, which is essential for high-contrast two-photon fluorescence microscopy, capable of deep-tissue optical penetration with minimized background autofluorescence and scattering.[13] Importantly, the formation of molecular aggregates, which can be beneficial for achieving robust and high-contrast imaging, can also be exploited through appropriate molecular

[a] *Department of Polymer Chemistry and Technology, Kaunas University of Technology, K. Barsausko St. 59, LT-50254, Kaunas, Lithuania. E-mail: rasa.keruckiene@ktu.lt*
[b] *National Institute of Research and Innovation, Riga, LV-1006, Latvia*
[c] *Department of Physics, National Taiwan University, 1, Sec. 4, Roosevelt Rd., Taipei 10617, Taiwan*

design to overcome aggregation-caused quenching (ACQ) and promote efficient emission.[14]

In this regard, aggregation-induced emission (AIE) can counteract ACQ, while appropriately engineered D–A systems can further exploit aggregation to promote reverse intersystem crossing (RISC) and activate AIDF. In particular, intermolecular CT interactions and controlled molecular packing can reduce ΔE_{ST} and facilitate RISC, highlighting the importance of structural organization in achieving efficient AIDF.[15–18] The cationic centre can further modulate these interactions by altering molecular packing, electronic coupling, and excited-state dynamics, thereby strongly influencing whether aggregation leads to enhanced or quenched emission.[19] Cation formation through *N*-alkylation provides an effective means of modifying the electronic structure and intermolecular interactions of pyridine-based luminophores.[19,20] However, cationization does not intrinsically promote AIE or delayed emission. Its' effect depends strongly on molecular architecture and the resulting balance between electronic coupling, conformational flexibility, and aggregation.[21] This is particularly relevant for AIDF systems, where cationization may either facilitate or disrupt the structural and electronic conditions required for delayed fluorescence.

To elucidate these effects, we synthesized a twisted pyridine-based compound (**PyAcr**) and its cationic pyridinium analogue (**PyAcr**$^+$) and investigated their optical, two-photon, and time-resolved emission properties. **PyAcr** exhibits AIDF accompanied by strong two-photon-excited fluorescence, whereas **PyAcr**$^+$ displays substantially weaker emission. This contrasting behaviour demonstrates that cationization alone is insufficient to generate an emissive aggregated state and highlights the importance of molecular architecture in controlling aggregation and excited-state dynamics. These structure–property relationships provide a basis for understanding how rational structural modification can be exploited to tune the optical response of organic luminophores for advanced imaging applications.

Results and discussion

Synthesis and thermal properties

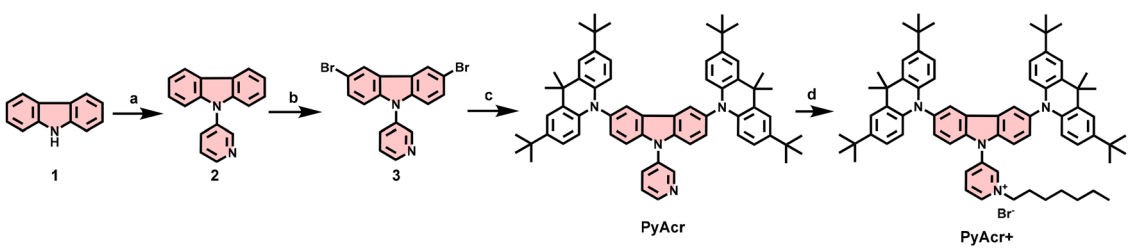
The synthetic route to the pyridine-based dimethylacridan **PyAcr** involves a four-step synthesis (Scheme 1). First, 9*H*-carbazole **1** was converted into 9-(pyridin-3-yl)-9*H*-carbazole **2** by a Pd-catalyzed Buchwald–Hartwig cross-coupling reaction with 3-bromopyridine.[22,23] The obtained carbazole **2** was brominated with NBS under mild conditions following a reported procedure,[24] and the resulting brominated intermediate **3** was reacted with 2,7-di-*tert*-butyl-9,9-dimethyl-9,10-dihydroacridine to afford **PyAcr** in 65% yield. Alkylation of **PyAcr** with 1-bromoheptane afforded pyridinium salt **PyAcr**$^+$ in a 90% yield. The structures and the purity of all the final compounds were confirmed by ^{1}H and ^{13}C NMR spectroscopy (Fig. S1), high resolution mass spectrometry (Fig. S2), and elemental analysis. **PyAcr** was found to be soluble in toluene, acetone, ethyl acetate, and chloroform, while **PyAcr**$^+$ was mainly soluble in water.

Differential scanning calorimetry (DSC) and thermogravimetric analysis (TGA) under a nitrogen atmosphere were used to study the morphological transitions and thermal stability of **PyAcr** and **PyAcr**$^+$ (Table 1 and Fig. S3a–c). The TGA measurement revealed that the pyridine-based compound **PyAcr** exhibited relatively high thermal stability of 393 °C. Both **PyAcr** and **PyAcr**$^+$ were obtained as crystalline materials with their melting temperatures of 336 °C and 200 °C observed during the 1st DSC scans (Fig. S3b and c). Subsequently, the glass transition temperature (T_G) for the compound **PyAcr**$^+$ was observed to be 171 °C.

Electrochemical properties and theoretical calculations

The electrochemical properties of **PyAcr** were analyzed using cyclic voltammetry (Fig. S3d). The compound exhibited a fully reversible single oxidation wave with an oxidation onset ($E_{oxonset}$) value of 0.31 V *vs.* Fc/Fc$^+$ for **PyAcr** up to 1 eV. Electrochemical oxidation of **PyAcr** was found to be attributed to the presence of the same 2,7-di-*tert*-butyl-acridine donor fragment. Therefore, *tert*-butyl groups not only lower the oxidation potential, but also are responsible for the reversibility of the oxidation process of the **PyAcr** compound. Due to the low solubility of **PyAcr**$^+$ in organic solvents, voltammograms of sufficient quality were not obtained.

DFT calculations were employed to gain a deeper insight into the structure–property relationships of **PyAcr** and **PyAcr**$^+$ (Fig. 1). In the optimized ground state geometries, the dihedral angles between the central carbazole and peripheral dimethylacridan moieties were estimated to be 90°. Whereas those between the acceptor pyridine moiety and the central carbazole moiety were calculated to be around 36°.



Scheme 1 Synthetic routes for compounds **PyAcr** and **PyAcr**$^+$. Reagents and conditions: (a) 3-bromopyridine, $Pd_2(dba)_3$, NaO*t*Bu, XPhos, 110 °C, 24 h, 65%. (b) NBS, DMF, 0 °C to rt, 24 h, 90%. (c) 2,7-Di-*tert*-butyl-9,9-dimethyl-9,10-dihydroacridine, $Pd_2(dba)_3$, NaO*t*Bu, XPhos, 110 °C, 24 h, 65%. (d) 1-Bromoheptane, EtOH, reflux, 2 h, 90%.

 This journal is © the Owner Societies 2026

Table 1 Thermal characteristics of **PyAcr** and **PyAcr**$^+$

Compound	$T_{D\text{-}5\%}$, °C	T_M, °C	T_G, °C
PyAcr	368	336	—
PyAcr$^+$	393	200	171

$T_{D\text{-}5\%}$ – decomposition temperature; T_M – melting temperature; T_G – glass transition temperature.

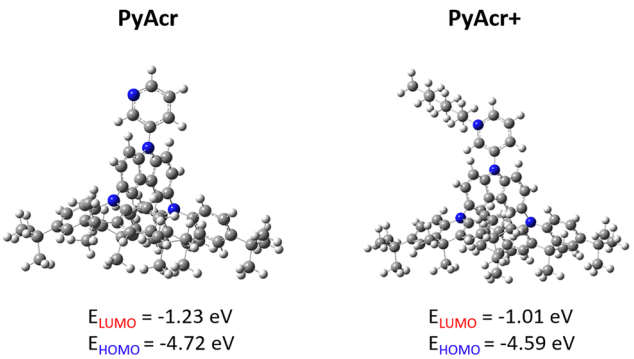


Fig. 1 Optimized ground state geometries under vacuum at the B3LYP/6-31++G level of theory of **PyAcr** and **PyAcr**$^+$.

The twisted geometries of **PyAcr** and **PyAcr**$^+$ controls the conjugation length, prevents severe π–π stacking, and facilitates minimal HOMO and LUMO overlap (Fig. S4). Accordingly, the calculated HOMO and LUMO values (Fig. 1) display similar CT capabilities for both emitters. Likewise, the electronic structures of **PyAcr** and **PyAcr**$^+$ are also similar, with HOMOs mainly located on the electron donating peripheral dimethylacridan moieties, and the LUMOs situated on the acceptor pyridine/pyridinium fragment. The calculated ground-state dipole moments (2.91D for **PyAcr** and 6.16D for **PyAcr**$^+$) indicate greater molecular polarity of alkylated pyridine compound **PyAcr**$^+$.

Calculations of the dominant transitions at the first singlet excited state of **PyAcr** and **PyAcr**$^+$ were performed to compare with their ground-state geometry (Fig. S4a). The conformational stability in the excitation process of **PyAcr** is significant for the control of energy losses and for inducing efficient intramolecular CT. TD-DFT calculations predict that the dominant S_1 transition is CT in nature. The dominating distributions show transition from donor fragments towards acceptor moieties.

Optical properties

UV/Vis absorption and emission spectra of toluene solutions at *ca.* 10^{-5} M concentration of **PyAcr** and **PyAcr**$^+$ were measured in ambient atmosphere (Fig. 2 and Table 2). Both **PyAcr** and **PyAcr**$^+$ showed strong π → π* absorption in the 280–300 nm region and a weak CT band in the 350–400 nm region. The absorption of **PyAcr** was weaker in the CT region as compared to that of **PyAcr**$^+$, which is expected due to the stronger electron accepting ability of the pyridinium subunit and ground state dipole moment. Such features indicate different electronic coupling in the ground state, which could result in a significant change in photoluminescence (PL) features.

The toluene solutions of **PyAcr** and **PyAcr**$^+$ showed narrow single emission bands with maxima at 426 nm. The structured PL peaks indicate emission from a locally excited state (LE). This was further confirmed by time-resolved spectroscopy (see Fig. S5 and Table 2), as the mono-exponential PL lifetimes did not exceed 6 ns.

It was observed that **PyAcr** and **PyAcr**$^+$ showed enhanced solid-state emission as compared to their respective toluene solutions (Table 2), in which the dispersed and solvated molecules commonly exhibit poor emission efficiency due to the active non-radiative decay pathways. Thus, to establish whether the more emissive CT state is activated in the aggregates, aggregation induced emission (AIE) studies were carried out on THF solutions with varying water fractions (0–99%) for **PyAcr** and hexane fractions for **PyAcr**$^+$. Emission spectra were recorded at different water contents to monitor changes in PL intensity and peak position, allowing assessment of the compounds' AIE characteristics. The PL spectra of compound **PyAcr** remained mostly constant until the water fraction reached 60%. Upon addition of 70–80% water, the intensity of CT emission at 445 nm increased significantly (Fig. 3a).

Since **PyAcr**$^+$ is soluble in water, the aggregation experiments were conducted for THF/hexane mixtures. The increase in the hexane fraction rapidly decreased the PL intensity of **PyAcr**$^+$ at

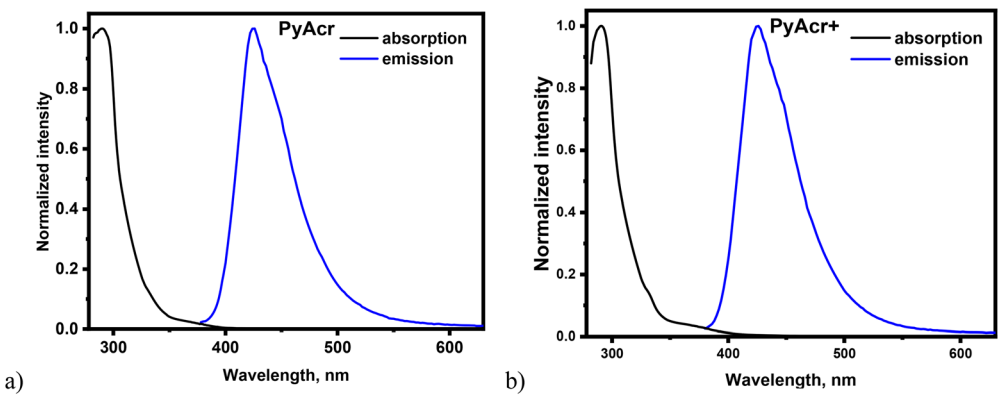


Fig. 2 Absorption and photoluminescence spectra of the toluene solutions of **PyAcr** (a) and **PyAcr**$^+$ (b). λ_{exc} = 330 nm.

Table 2 Photophysical parameters of **PyAcr** and **PyAcr**$^+$

Compound	λ_{abs},[a] nm	λ_{PL},[a] nm	PLQY,[a] %	τ_1,[a] ns	$\chi^{2\,a}$	S_1,[b] eV	T_1,[b] eV	ΔE_{ST}, eV
PyAcr	290	426	4/27[c]	5.50	1.078	3.272	3.139	0.133
PyAcr$^+$	290	426	0/2[c]	5.55	1.039	3.196	3.122	0.074

[a] Toluene solutions. [b] THF solutions at 77 K. [c] Measured thin films of the target compounds.

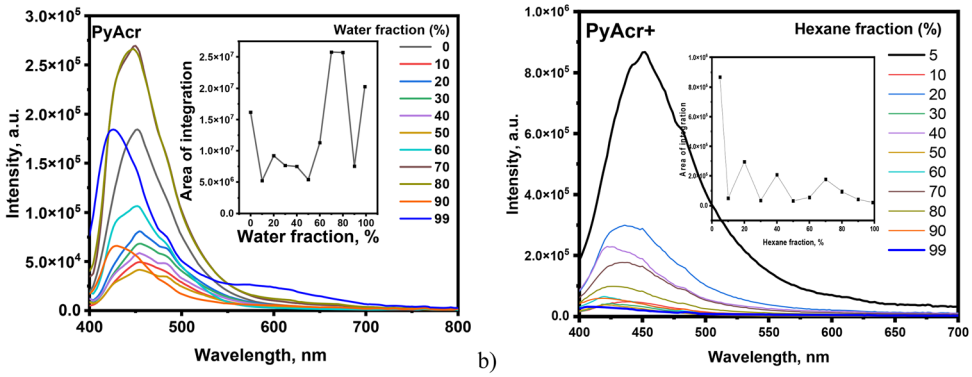


Fig. 3 Photoluminescence emission intensity spectra under aggregation conditions of the dispersions of **PyAcr** (a) in THF/water mixtures and **PyAcr**$^+$ (b) in THF/hexane mixtures. λ_{exc} = 330 nm.

448 nm (Fig. 3b). For **PyAcr**$^+$, significantly lowered emission intensity was observed starting from 10% hexane fraction. Thus, the aggregation experiments indicate that the poor plane-to-plane stacking, characteristic for compounds with twisted geometries, as established by the theoretically optimized molecular geometries (Fig. 1), suppressed intermolecular π–π stacking in compound **PyAcr**, thus enabling AIE. With increasing water fraction, the emission intensity of **PyAcr** initially decreases, followed by a pronounced enhancement at high water contents, consistent with the onset of aggregation-induced delayed fluorescence. The highly aqueous samples also exhibit a slight hypsochromic shift of the emission maximum (Fig. S6). This spectral change suggests that aggregation modifies the excited-state character and intermolecular packing, potentially reducing the contribution of the twisted CT state. Thus, such emission response reflects the competition between solvent-dependent excited-state relaxation and aggregation-induced restriction of intramolecular motions. In contrast, the suppression of plane-to-plane stacking in **PyAcr**$^+$ led to aggregation caused quenching, due to the lack of AIE-promoting intermolecular π^+–π interactions. Additionally, this might be influenced by high molecular polarity inducing non-radiative decay. Overall, these results confirm that, in the absence of intermolecular π–π stacking, restriction of molecular motion is sufficient to achieve AIE in non-cationic luminophores, while the lack of intermolecular π^+–π interactions in aggregates renders pyridinium salts less emissive.

Furthermore, the AIE studies show that the addition of polar solvent and restriction of intermolecular interactions successfully activates the CT state in **PyAcr**. Accordingly, the THF solution containing 70% water fraction of **PyAcr** was further investigated (Fig. 3). Following the evacuation of the aforementioned solution, the PL intensity of **PyAcr** increased by a factor of *ca.* 1.41. To verify the origin of aggregate-state emission, absorption was recorded under aggregation conditions (Fig. S7). The close agreement between the UV/Vis absorption and emission spectra of the **PyAcr** aggregates and neat film suggests similar intermolecular packing and excited state environment leading to efficient intermolecular CT. The similar second PL shoulder at longer wavelengths could be attributed to potential excimer formation. To further confirm the origin of CT emission, time-resolved PL study of the deoxygenated THF/water solution of **PyAcr** was performed. The sample exhibited significantly increased lifetime reaching ∼1 μs (Fig. 4b). Such emission is characteristic of delayed emission (DF) suggesting that **PyAcr** exhibits AIDF. Photoluminescence and phosphorescence spectra of solid THF solutions at 77 K were recorded to evaluate the singlet–triplet energy splitting values. The prompt and 1 ms-delayed PL spectra (Fig. S8) closely overlapped, with energy splitting values of 0.13 eV for **PyAcr** and 0.074 eV for **PyAcr**$^+$. These small singlet–triplet energy splitting values demonstrate that the locked donor–acceptor conformations intrinsically possess a narrow singlet–triplet gap favourable for RISC. Because room-temperature solutions exhibit short-lived prompt fluorescence (<6 ns, Table 2), aggregate formation plays the crucial role of suppressing non-radiative deactivation channels to enable thermally activated delayed fluorescence (AIDF). The significantly increased PLQY of the THF/water solution of **PyAcr** to 45% makes this material promising for bioimaging applications. These observations highlight the influence of solvent polarity and oxygen concentration on the photophysical properties of **PyAcr**.

The theoretical calculations provided insight into the intrinsic electronic structure and charge-transfer character of **PyAcr**, while the experimentally observed AIDF behavior is associated

 This journal is © the Owner Societies 2026

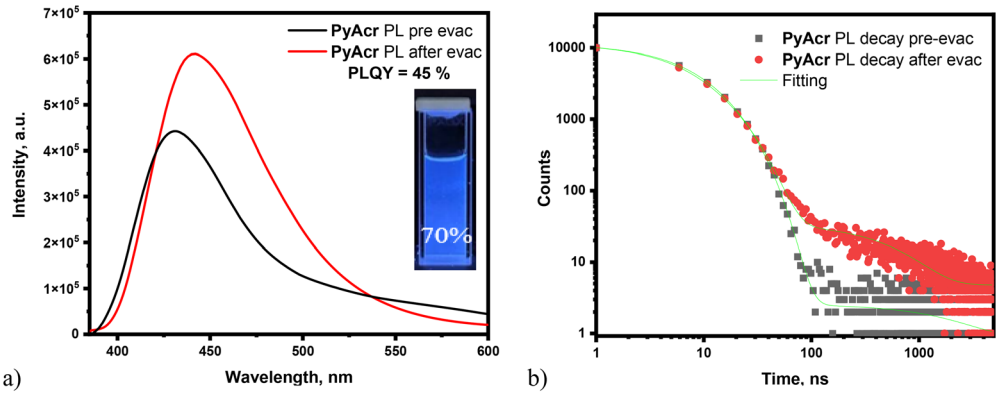


Fig. 4 PL spectra (a) and PL decay curves (b) of the evacuated and non-evacuated dispersion of **PyAcr** in a THF/water (70%) mixture. λ_{exc} = 330 nm. The inset shows the tested sample under UV excitation.

with the changes induced upon aggregation. The calculated values of singlet triplet energy values of both compounds are also quite low (see Fig. S4b). The calculated energy gaps between the singlet and triplet states (ΔE_{ST}) for both compounds are less than 0.34 eV, providing a relatively small energetic barrier for singlet triplet state conversion. Such spin conversion can be facilitated by spin–orbit coupling (SOC), with the magnitude of the SOC matrix element (SOCME) reflecting the extent of spin–orbit interaction between the corresponding excited states. The calculated SOCME values between the lowest three singlet and triplet excited states indicate non-negligible spin–orbit coupling and, together with the small ΔE_{ST}, suggest favorable conditions for intersystem crossing and reverse intersystem crossing. These results provide theoretical support for the involvement of triplet states in the observed delayed emission. The theoretically calculated SOC value for the S_1–T_1 transition is 1.13 cm^{-1} for **PyAcr**, and 0.06 cm^{-1} for **PyAcr**$^+$. The similar SOC values of the upper states of **PyAcr**$^+$ show potential triplet population from the higher states. This might allow several RISC channels to emerge from higher-lying states. Rather, the high SOC value for the S_1–T_1 transition of **PyAcr** enables this observed RISC channel and the subsequent DF seen in the aggregated state.

Bioimaging potential *via* TPEF

TPEF microscopy was used to visualize the AIE distribution and to evaluate the bioimaging potential of **PyAcr** and **PyAcr**$^+$, revealing a clear difference in emission visibility between the two compounds (Fig. 5a). For the AIE-active **PyAcr**, numerous fluorescent aggregates were readily observed across the field of view, indicating that aggregation effectively activates TPEF emission. In contrast, **PyAcr**$^+$ generally exhibited very weak fluorescence under the same imaging conditions, with detectable signals appearing only from rare large clusters. Brightness histogram analysis further supports this observation, showing that most **PyAcr**$^+$ aggregates remain weakly emissive, while only a few rare bright events contribute to the high-intensity tail of the distribution (yellow arrow). This is consistent with ACQ, in which aggregate formation suppresses emission efficiency and makes most **PyAcr**$^+$ aggregates difficult to detect by two-photon microscopy.

The advantage of TPEF in tissue inspection originates from its nonlinear power dependency, which enables intrinsic optical sectioning capability. In Fig. 5b, we checked the two-photon nature by measuring the fluorescence intensity as a function of excitation power at 710 nm. The log–log plot showed a quadratic power dependence, confirming that the observed fluorescence originates from a two-photon absorption process. We further examined the excitation-wavelength dependence of the TPEF intensity for both **PyAcr** and **PyAcr**$^+$ within the accessible tuning range of our Ti: sapphire laser (Fig. 5c). Since **PyAcr**$^+$ exhibits relatively weak emission, background contributions may make the normalized wavelength dependence appear flatter than that of **PyAcr**. Nevertheless, both the strongest emission peaks were observed at 710 nm, the lower tunable limit of our laser system, indicating that the TPEF intensity increases toward shorter excitation wavelengths. Based on the one-photon absorption band near 300 nm, the actual TPEF maxima are expected to lie at approximately 600 nm. Importantly, strong TPEF signals can still be obtained at 710 nm, which lies within the first near-infrared biological window,[25] supporting the potential of these materials for two-photon bioimaging.

Conclusions

Overall, this experimental and theoretical study demonstrates that controlled modulation of molecular charge, through the conversion of a neutral pyridine into its cationic pyridinium analogue, provides an effective means of tuning excited-state properties and aggregation behavior. The π-extended pyridine–dimethylacridan derivatives exhibit high thermal stability, with onset temperatures of thermal degradation exceeding 360 °C, together with good electrochemical stability and small singlet–triplet energy gaps of 0.07–0.13 eV. Importantly, the direct comparison of the neutral **PyAcr** and cationic **PyAcr**$^+$ derivatives reveals that cationization substantially alters the balance between charge-transfer character,

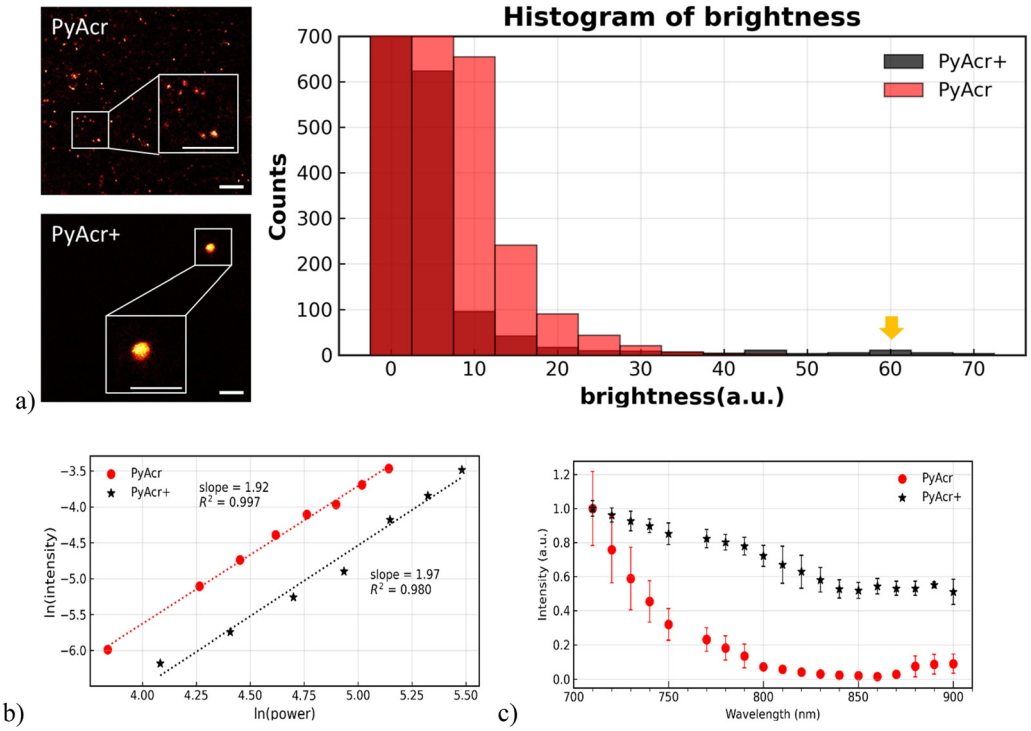


Fig. 5 (a) Histogram analysis and TPEF images for aggregated molecules **PyAcr** and **PyAcr**$^+$. The inset shows the enlarged view for selected aggregations. (b) Power dependence for TPEF characterization. (c) Normalized two-photon excitation spectrum measurements. Scale bar: 20 μm.

molecular interactions, and aggregation. While neutral **PyAcr** exhibits pronounced aggregation-induced emission, a high photoluminescence quantum yield of 45%, and strong two-photon-excited fluorescence under near-infrared excitation, cationic **PyAcr**$^+$ does not retain the AIE behavior and shows substantially weaker emission. These results demonstrate that cationization alone is insufficient to enhance luminescence, and that the resulting photophysical response is governed by the interplay between charge distribution, molecular conformation, electronic coupling, and aggregation. Thus, the neutral-to-cationic pyridine design strategy provides valuable structure–property insights for rationally controlling emission switching and excited-state dynamics, and highlights **PyAcr** as a promising platform for two-photon bioimaging and other environment-responsive optoelectronic applications.

Author contributions

Rasa Keruckiene: conceptualization, validation, and writing (review and editing); Kaspars Leduskrasts: methodology, formal analysis, and writing (original draft); Ho-Chia Tsai: formal analysis and methodology; Mariia Stanitska: methodology and validation; Daiana Ospanova: methodology and data curation; Dmytro Volyniuk: validation and writing (review and editing); Edgars Suna: validation, data curation, and writing (review and editing); Shi-Wei Chu: validation; Juozas V. Grazulevicius: supervision.

Conflicts of interest

The authors declare no competing financial interest.

Data availability

The data supporting this article have been included as part of the supplementary information (SI). Supplementary information is available. See DOI: https://doi.org/10.1039/d6cp02166b.

Acknowledgements

This work was supported by the project of the scientific cooperation program between Latvia, Lithuania and Taiwan, "Synthesis and characterization of new organic emitters exhibiting long-lived emission for brain imaging (SYNERGISM)," funded by the Research Council of Lithuania (LMTLT) under agreement no. S-LLT-24-4. Dr E. Skuodis is acknowledged for the TGA and DSC measurements, and PhD student Melika Ghasemi is acknowledged for assistance in photophysical measurements.

References

1 L. Xu, Y. Mo, N. Su, C. Shi, N. Sun, Y. Zhang, L. Duan, Z.-H. Lu and J. Ding, D–O–A based organic phosphors for both aggregation-induced electrophosphorescence and host-free sensitization, *Nat. Commun.*, 2023, **14**, 1678.

 This journal is © the Owner Societies 2026

2 H.-T. Feng, J. Zeng, P.-A. Yin, X.-D. Wang, Q. Peng, Z. Zhao, J. W. Y. Lam and B. Z. Tang, Tuning molecular emission of organic emitters from fluorescence to phosphorescence through push-pull electronic effects, *Nat. Commun.*, 2020, **11**, 2617.

3 A. Szukalski, B. Sahraoui, B. Kulyk, C. A. Lazar, A. M. Manea and J. Mysliwiec, Chemical structure versus second-order nonlinear optical response of the push–pull type pyrazoline-based chromophores, *RSC Adv.*, 2017, **7**, 9941–9947.

4 Y. Yang, X. Zhang, Z. Hu and Y. Wu, Organic Nonlinear Optical Crystals for Highly Efficient Terahertz-Wave Generation, *Crystals*, 2023, **13**, 144.

5 Y. Zheng, P. Cheng, X. Qian, J. Guan, R. Shi, M. Xin, J. Xu and X.-H. Bu, Self-assembled organic nonlinear optical crystals based on pyridine derived fluorenone, *Mater. Chem. Front.*, 2023, **7**, 698–704.

6 X. Tian, L. C. Murfin, L. Wu, S. E. Lewis and T. D. James, Fluorescent small organic probes for biosensing, *Chem. Sci.*, 2021, **12**, 3406–3426.

7 Y. Yang, F. Gao, Y. Wang, H. Li, J. Zhang, Z. Sun and Y. Jiang, Fluorescent Organic Small Molecule Probes for Bioimaging and Detection Applications, *Molecules*, 2022, **27**, 8421.

8 G. Zerbib, A. Roux, L. Salat, F. Cisnetti, D. Boyer, G. Chadeyron and F. Leroux, A triazolium-based fluorophore intercalated in layered double hydroxides: from simple syntheses to bright solid-state luminescence, *Dalton Trans.*, 2024, **53**, 9369–9379.

9 E. Taipale, N. A. Durandin, J. K. Salunke, N. R. Candeias, T.-P. Ruoko, J. S. Ward, A. Priimagi and K. Rissanen, Protonation-induced fluorescence modulation of carbazole-based emitters, *Mater. Adv.*, 2022, **3**, 1703–1712.

10 K. Leduskrasts and E. Suna, Intermolecular Charge-Transfer Luminescence by Self-Assembly of Pyridinium Luminophores in Solutions, *ChemistryOpen*, 2021, **10**, 1081–1086.

11 D. Jelisejevs, A. Bundulis, A. Sapne and K. Leduskrasts, Through-space cation–π quadrupole–monopole design enables selective suppression of third-order nonlinear optical Kerr effects, *J. Mater. Chem. C*, 2026, **14**, 10805–10812.

12 A. Cesaretti, A. Spalletti, F. Elisei, P. Foggi, R. Germani, C. G. Fortuna and B. Carlotti, The role of twisting in driving excited-state symmetry breaking and enhanced two-photon absorption in quadrupolar cationic pyridinium derivatives, *Phys. Chem. Chem. Phys.*, 2021, **23**, 16739–16753.

13 Q. Lu, C.-J. Wu, Z. Liu, G. Niu and X. Yu, Fluorescent AIE-Active Materials for Two-Photon Bioimaging Applications, *Front. Chem.*, 2020, **8**, 617463.

14 Y. Xing, Q. Li, L. Chen, Y. Yang, S. Yu and L. Zhang, Thermally Activated Delayed Fluorescence in Aqueous Solution: Preparation, Performance, and Biomedical Application, *Adv. Funct. Mater.*, 2026, **36**, e32124.

15 D. Barman and P. K. Iyer, Aggregation-Induced Delayed Fluorescence and Phosphorescence from Hot Excitons via Suppression of Kasha's Rule in a Stimuli-Active Molecular Rotor, *J. Phys. Chem. C*, 2023, **127**, 2694–2704.

16 B. Zhang, Y. Kong, H. Liu, B. Chen, B. Zhao, Y. Luo, L. Chen, Y. Zhang, D. Han, Z. Zhao, B. Z. Tang and L. Niu, Aggregation-induced delayed fluorescence luminogens: the innovation of purely organic emitters for aqueous electrochemiluminescence, *Chem. Sci.*, 2021, **12**, 13283–13291.

17 M. Upadhyay and D. Ray, Regulation of aggregation-enhanced thermally activated delayed fluorescence in butterfly-shaped donor–acceptor conjugates, *Chem. Commun.*, 2025, **61**, 5015–5018.

18 W. Zhang, S. Li, Y. Gong, J. Zhang, Y. Zhou, J. Kong, H. Fu and M. Zhou, Aggregation Enhanced Thermally Activated Delayed Fluorescence through Spin-Orbit Coupling Regulation, *Angew. Chem., Int. Ed.*, 2024, **63**, e202404978.

19 A. Klimash, A. Prlj, D. S. Yufit, A. Mallick, B. F. E. Curchod, P. R. McGonigal, P. J. Skabara and M. K. Etherington, From phosphorescence to delayed fluorescence in one step: tuning photophysical properties by quaternisation of an sp^2-hybridised nitrogen atom, *J. Mater. Chem. C*, 2022, **10**, 9484–9491.

20 A. T. Turley, A. Danos, A. Prlj, A. P. Monkman, B. F. E. Curchod, P. R. McGonigal and M. K. Etherington, Modulation of charge transfer by *N*-alkylation to control photoluminescence energy and quantum yield, *Chem. Sci.*, 2020, **11**, 6990–6995.

21 K. Leduskrasts and E. Suna, Aggregation induced emission in one easy step: pyridinium AIEgens and counter ion effect, *RSC Adv.*, 2020, **10**, 38107–38113.

22 K. Leduskrasts, A. Kinens and E. Suna, The emission efficiency of cationic solid state luminophores is directly proportional to the intermolecular charge transfer intensity, *Chem. Commun.*, 2023, **59**, 6905–6908.

23 J. K. Kwon, J. H. Cho, Y. S. Ryu, S. H. Oh and E. K. Yum, N-Arylation of carbazole by microwave-assisted ligand-free catalytic CuI reaction, *Tetrahedron*, 2011, **67**, 4820–4825.

24 M. S. Park and J. Y. Lee, 9-(Pyridin-3-yl)-9*H*-carbazole derivatives as host materials for green phosphorescent organic light-emitting diodes, *Org. Electron.*, 2013, **14**, 1291–1296.

25 X. Liu, T. Zhang, T. Ni, N. Jiang, Z. Liu, Z. Bian, Z. Lu and C. Huang, Co-deposited Cu(I) Complex for Tri-layered Yellow and White Organic Light-Emitting Diodes, *Adv. Funct. Mater.*, 2014, **24**, 5385–5392.